



# Pendulum models of ponytail motion during walking and running

Raymond H. Plaut<sup>a</sup>, Lawrence N. Virgin<sup>b,\*</sup>

<sup>a</sup> Department of Civil and Environmental Engineering, Virginia Tech, Blacksburg, VA 24061, USA

<sup>b</sup> Department of Mechanical Engineering and Materials Science, Duke University, Durham, NC 27708, USA

## ARTICLE INFO

### Article history:

Received 11 June 2012

Received in revised form

1 February 2013

Accepted 13 February 2013

Handling Editor: J. Macdonald

Available online 16 March 2013

## ABSTRACT

Steady-state motions of a woman's ponytail during level, straight, walking and running are examined. Based on reported data, formulas have been developed for the relationship of the forward speed to the frequencies of vertical and sideways motion of the head, and of the form of that motion. The ponytail is modeled as a compound pendulum or a multi-bar pendulum with 2, 3, or 5 rigid bars. Motions in the vertical plane perpendicular to the direction of progression are analyzed. Rotational springs and dashpots are placed at the joints, and aerodynamic damping (air drag) is included. Attention is focused on the variation of the amplitudes of the bars as the woman's walking speed and then running speed increase. An example of three-dimensional motions of a spherical-pendulum model also is included. Experiments were conducted on a double pendulum with parabolic applied motion at the top. The damping is modeled by rotational friction (i.e., a constant resisting moment at the top and internal joints), and the numerical results agree well with the test data.

© 2013 Elsevier Ltd. All rights reserved.

## 1. Introduction

Keller [1] analyzed the motion of the ponytail of a jogging woman as a stability problem. He assumed that the jogger's head oscillates vertically, and modeled the ponytail as either a rigid pendulum or a flexible string. In those cases, the ponytail remains in a vertical configuration until that state becomes unstable, and then the ponytail sways from side to side.

However, observations of the motion of the back of a person's head during walking or running show that lateral (medial-lateral, sideways) motion occurs as well as vertical motion. This leads to a “response problem” rather than a “stability problem.” During walking, the motion of the head in the plane that is perpendicular to the direction of jogging (coronal plane, frontal plane) forms a Lissajous figure, like a sideways (lazy) figure eight with the sides pushed upward. During running, the motion may resemble a U shape.

In the present study, the ponytail will usually be modeled as a pendulum with one rigid bar or multiple rigid bars. In most of the cases, motion will be restricted to the coronal plane. One example will involve a spherical (spatial) pendulum and its three-dimensional motion. Experimental results will be presented for a double pendulum in the coronal plane.

In Section 2, motions of the head will be discussed. The equations of motion for a compound pendulum with  $n$  rigid bars and pinned joints will be presented in Section 3. Rotational springs and dashpots at the joints will be included, along with

\* Corresponding author. Tel.: +1 919 660 5342; fax: +1 919 660 5219.

E-mail addresses: [rplaut@vt.edu](mailto:rplaut@vt.edu) (R.H. Plaut), [l.virgin@duke.edu](mailto:l.virgin@duke.edu) (L.N. Virgin).

aerodynamic damping. The planar responses for models with one, three, and five bars will be analyzed in Sections 4, 5, and 6, respectively. A spherical pendulum with a concentrated mass will be analyzed in Section 7, the experimental results will be presented in Section 8, and concluding remarks will be given in Section 9.

## 2. Kinematic characteristics of walking and running

The formulas to be adopted for head motions are developed in Ref. [2]. The “step time” is the length of time between initial contact of one foot with the ground and subsequent initial contact of the other foot with the ground, and the step rate  $f$  is the reciprocal of the step time. Often  $f$  is called the cadence, especially if its units are steps per minute. Here, numerical values of  $f$  will be in steps per second (steps/s), which is often used in reported data. The average walking or running speed (sometimes called velocity) will be denoted  $V$ , with numerical values in m/s.

For women in the walking range (assumed to be  $f \leq 2.9$ ), it is assumed that

$$f = 1.8V^{0.6}. \quad (1)$$

In the running range ( $f > 2.9$ ), it is assumed that

$$f = 1.2 + 0.54V - 0.015V^2. \quad (2)$$

The excitation for the ponytail consists of the motion at the top of the ponytail, assumed to be located at or near the center of the back of the head. The total lateral excursion of the top of the ponytail in the coronal plane will be denoted  $2A$ , and the total vertical excursion will be  $2B$ .

Based on data in the literature, functions were postulated for  $A$  and  $B$  in terms of step frequency  $f$  [2]. The assumed functions are fourth-order polynomials given by

$$A = 3 + 0.03f - 0.65f^2 + 0.206f^3 - 0.0186f^4, \quad (3)$$

$$B = 0.063 - 0.0217f + 1.08f^2 - 0.365f^3 + 0.033f^4, \quad (4)$$

with  $f$  in steps/s and  $A$  and  $B$  in cm. The amplitude  $A$  decreases with  $f$ , whereas  $B$  increases until  $B = 2.55$  cm at  $f = 3.20$  steps/s, and then  $B$  decreases.

Motions of the head at the top of the ponytail in the coronal plane are assumed here. Let  $T$  denote time (in seconds),  $X(T)$  the horizontal (sideways) motion (in cm), positive if to the right when viewing the back of the head,  $Y(T)$  the vertical motion (in cm), positive if downward, and  $\Omega$  the angular frequency for steps (in radians/s). The functions  $X(T)$  and  $Y(T)$  are chosen to be [2]

$$X(T) = A \sin(\Omega T + \beta), \quad Y(T) = -B \sin(2\Omega T), \quad (5)$$

where  $\Omega = \pi f$ . The frequency  $\Omega$  for vertical motion (i.e., for steps) is twice that for sideways motion. The phase  $\beta$  is chosen to have the value 1 for  $f \leq 2.9$  and 0.8 for  $f > 2.9$ .

Associated Lissajous figures for  $f = 1, 2$ , and 3 are depicted in Ref. [2]. When the excitation frequency  $\Omega$  is equal to a natural frequency of the linearized, unforced, undamped system, both primary external resonance (due to  $X$ ) and principal parametric resonance (due to  $Y$ ) exist [3].

## 3. Equations of motion for $n$ -bar compound pendulum

Assume that the ponytail is modeled by a multiple compound pendulum with  $n$  uniform rigid bars, pinned at the top and between adjacent bars. Motions are in the coronal plane, with excitation at the top given by Eq. (5). Subscript 1 will refer to the top bar, and  $n$  to the bottom bar.

The  $j$ th bar has length  $L_j$ , mass  $m_j$ , and rotation angle  $\theta_j(T)$  from the vertical (positive if counter-clockwise when viewed from the back). The total length of the  $n$ -bar pendulum is  $L$  and the total mass is  $m$ . At the top of the top bar ( $j = 1$ ), there are a rotational spring with stiffness  $K_1$  and a rotational dashpot with damping coefficient  $C_1$ . Connecting the  $j$ th bar ( $2 \leq j \leq n$ ) with the bar above it are a rotational spring with stiffness  $K_j$  and a rotational dashpot with damping coefficient  $C_j$  (representing internal dissipation of energy).

External damping from the air is also considered. For light objects exhibiting slow motions, air drag may be assumed to be proportional to the rotational speed at each point along the model (i.e., viscous damping). The corresponding aerodynamic damping coefficient (per unit length) will be denoted  $D$ . The moment about the top support due to the air drag is discussed in Appendix A of Ref. [4].

A more realistic model of aerodynamic damping would also include a quadratic term that changes sign when the velocity changes direction, and possibly additional nonlinear terms [5,6]. However, for these compound pendulums with distributed mass, and for the spherical pendulum in Section 8, such nonlinear terms are difficult to analyze and will not be included. The effect of a quadratic damping term is examined in Appendix B of Ref. [4] for a simple pendulum.

It is convenient to define the quantities

$$\begin{aligned} Q_i &= \frac{1}{2}m_i + \sum_{j=i+1}^n m_j, \quad Q_{ij} = Q_{\max(i,j)} - \frac{1}{6}m_i\delta_{ij}, \\ R_i &= \frac{1}{2}L_i + \sum_{j=i+1}^n L_j, \quad R_{ij} = R_{\max(i,j)} - \frac{1}{6}L_i\delta_{ij}, \\ \theta_0 &= 0, \quad \dot{\theta}_0 = 0, \quad K_{n+1} = 0, \quad C_{n+1} = 0, \end{aligned} \quad (6)$$

where  $\delta_{ij}$  is the Kronecker delta.

The governing equations of motion, with  $i = 1, 2, \dots, n$ , are

$$\begin{aligned} L_i \sum_{j=1}^n Q_{ij} L_j [\ddot{\theta}_j \cos(\theta_i - \theta_j) + \dot{\theta}_j^2 \sin(\theta_i - \theta_j)] + Q_i L_i [\ddot{X} \cos \theta_i + (g - \ddot{Y}) \sin \theta_i] + K_i (\theta_i - \theta_{i-1}) + K_{i+1} (\theta_i - \theta_{i+1}) + C_i (\dot{\theta}_i - \dot{\theta}_{i-1}) \\ + C_{i+1} (\dot{\theta}_i - \dot{\theta}_{i+1}) + DL_i \sum_{j=1}^n R_{ij} L_j \dot{\theta}_j \cos(\theta_i - \theta_j) + DL_i R_i (\dot{X} \cos \theta_i - \dot{Y} \sin \theta_i) = 0, \end{aligned} \quad (7)$$

where an overdot denotes differentiation with respect to  $T$ . Some of the terms in these equations are given in Refs. [7,8], and related equations are presented in Refs. [9–11].

The numerical calculations are conducted in terms of the nondimensional variables

$$x = \frac{X}{L}, \quad y = \frac{Y}{L}, \quad k_j = \frac{K_j}{mgL}, \quad c_j = \frac{C_j}{mL\sqrt{Lg}}, \quad d = \frac{DL\sqrt{L}}{m\sqrt{g}}, \quad t = T\sqrt{\frac{g}{L}}, \quad \omega = \Omega\sqrt{\frac{L}{g}}. \quad (8)$$

For a “regular”  $n$ -bar compound pendulum with identical bars, so that  $L_j = L/n$  and  $m_j = m/n$  ( $j = 1, 2, \dots, n$ ), the governing nondimensional equations of motion, with  $i = 1, 2, \dots, n$ , are

$$\begin{aligned} \sum_{j=1}^n P_{ij} [(\ddot{\theta}_j + d\dot{\theta}_j) \cos(\theta_i - \theta_j) + \dot{\theta}_j^2 \sin(\theta_i - \theta_j)] + nG_i [(\ddot{x} + d\dot{x}) \cos \theta_i + (1 - \ddot{y} - d\dot{y}) \sin \theta_i] \\ + n^3 [k_i (\theta_i - \theta_{i-1}) + k_{i+1} (\theta_i - \theta_{i+1}) + c_i (\dot{\theta}_i - \dot{\theta}_{i-1}) + c_{i+1} (\dot{\theta}_i - \dot{\theta}_{i+1})] = 0, \end{aligned} \quad (9)$$

where

$$G_i = n + \frac{1}{2} - i, \quad P_{ij} = n + \frac{1}{2} - \max(i, j) - \frac{1}{6}\delta_{ij}, \quad (10)$$

and an overdot denotes differentiation with respect to  $t$ .

Initial conditions are chosen, and the equations of motion (9) are integrated numerically using the subroutine NDSolve in Mathematica. When a steady-state solution with constant amplitudes is obtained, the maximum values of  $\theta_j(t)$ , denoted  $\theta_{j,\max}$ , are determined numerically. Typically the initial conditions (displacements and velocities) are chosen to be zero, but sometimes other values are required to find large steady-state solutions. All the computed solutions are stable.

Based on observations, the maximum lateral ponytail motion tends to occur in the jogging range, at a speed somewhat above that for the walk-to-run transition (WRT). Therefore, in the numerical examples, the stiffnesses of the rotational springs will be chosen such that this property will occur (e.g., so the lowest natural frequency of the model will be above the frequency at the WRT). Also, the resistance to rotation is relatively high at the top of the ponytail, and the rotational stiffness there will be chosen to be higher than those between adjacent bars if  $n > 1$ . From observations, the maximum rotation at the end of a woman's ponytail is typically less than  $90^\circ$ , and the damping coefficients will usually be chosen so that this will be satisfied.

#### 4. Compound pendulum

A simple or compound pendulum with an oscillating support has been investigated in many papers and books (e.g., Refs. [12,13]). In this section, the ponytail is modeled as a uniform rigid bar ( $n=1$ ), as shown in Fig. 1. Subscripts on  $\theta_1, K_1, C_1, k_1$ , and  $c_1$  are ignored. The governing equation of motion for  $\theta(T)$ , from Eq. (7), is

$$\frac{1}{3}mL^2\ddot{\theta} + (C + \frac{1}{3}DL^3)\dot{\theta} + K\theta + \frac{1}{2}mL[\ddot{X} \cos \theta + (g - \ddot{Y}) \sin \theta] + \frac{1}{2}DL^2(\dot{X} \cos \theta - \dot{Y} \sin \theta) = 0. \quad (11)$$

In Fig. 2,  $\theta_{\max}$  is plotted in degrees versus the nondimensional sideways frequency  $\omega$  for  $k=0.5$ ,  $c=0.15$ , and both  $d=0$  and  $d=0.1$ . The assumed WRT occurs at  $\omega = 1.45$  and a discontinuity occurs at that frequency, with a sudden small drop in  $\theta_{\max}$ . The nondimensional natural frequency of the linearized, unforced, undamped system is  $\omega = \sqrt{1.5 + 3k} = 1.73$ . The end of the range,  $\omega = 2.5$ , corresponds to  $f=5$ .

All the motions corresponding to the maximum rotations in Fig. 2 are periodic with the period of the excitation (i.e., the period of the lateral motion of the head, which in nondimensional terms is  $2\pi/\omega$ ). This is also true for all subsequent numerical solutions.

The peak value of  $\theta_{\max}$  is  $86.3^\circ$  for  $d=0$  and occurs at  $\omega = 1.64$ . The case with aerodynamic damping ( $d=0.1$ ) has lower amplitudes. The peak is  $\theta_{\max} = 56.6^\circ$  at  $\omega = 1.71$ .

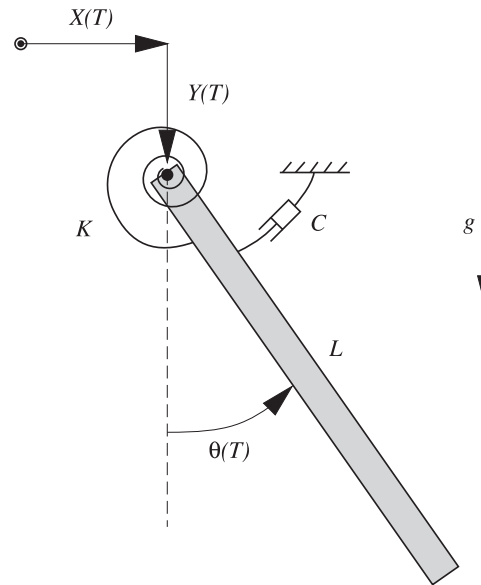


Fig. 1. Schematic of the compound pendulum.

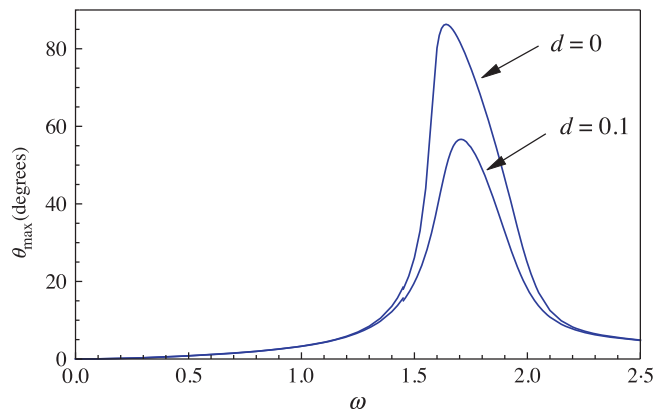


Fig. 2. Compound pendulum;  $\theta_{\max}$  vs. nondimensional sideways frequency  $\omega$  for  $k=0.5$ ,  $c=0.15$ ,  $d=0$  and  $0.1$ .

The direction of motion of the pendulum with respect to the sideways direction of motion of the head depends on the woman's speed. When viewed from behind, if the speed is low (e.g., in the walking range,  $\omega < 1.45$ ), the pendulum tends to be almost in-phase with the sideways motion  $X$  of the head, i.e.,  $\theta > 0$  when  $X > 0$ . As the running speed increases, the pendulum lags behind the horizontal head motion, with the phase lag increasing and becoming equal to  $142^\circ$  at  $\omega = 2.5$ .

If the dimensional stiffness and damping coefficients ( $K, C, D$ ) are fixed, and if either the total mass ( $m$ ) or the mass per unit length ( $m/L$ ) is fixed, then the peak value of  $\theta_{\max}$  increases if the length  $L$  is increased. If the mass per unit length is increased but all other dimensional quantities remain the same, again the peak value of  $\theta_{\max}$  increases.

## 5. Triple compound pendulum

A triple compound pendulum ( $n=3$ ) is analyzed in this section. The equations are obtained from Eq. (9). Numerical results are presented in Fig. 3 for three identical bars having  $L_1 = L_2 = L_3 = L/3 = 8.33$  cm,  $m_1 = m_2 = m_3 = m/3$ ,  $k_1 = 1$ ,  $k_2 = k_3 = 0.05$ ,  $c_1 = c_2 = c_3 = 0.1$ , and  $d=0.1$ . The nondimensional natural frequencies of the linearized, unforced, undamped system are  $\omega = 1.51$ ,  $5.00$ , and  $9.88$ .

In Fig. 3,  $\theta_{1,\max}$ ,  $\theta_{2,\max}$ , and  $\theta_{3,\max}$  are plotted versus  $\omega$ . The peak values of  $\theta_{1,\max}$ ,  $\theta_{2,\max}$ , and  $\theta_{3,\max}$  are  $16.3^\circ$ ,  $58.4^\circ$ , and  $71.4^\circ$ , respectively, at  $\omega = 1.61$ ,  $1.56$ , and  $1.57$ . For  $\omega < 1$ , the bar motions are almost in-phase with each other and with the lateral motion of the head. As  $\omega$  increases, the phase lags of the bars with the head motion increase, and at  $\omega = 2.5$  they are equal to  $61^\circ$ ,  $152^\circ$ , and  $173^\circ$  for  $\theta_1$ ,  $\theta_2$ , and  $\theta_3$ , respectively.

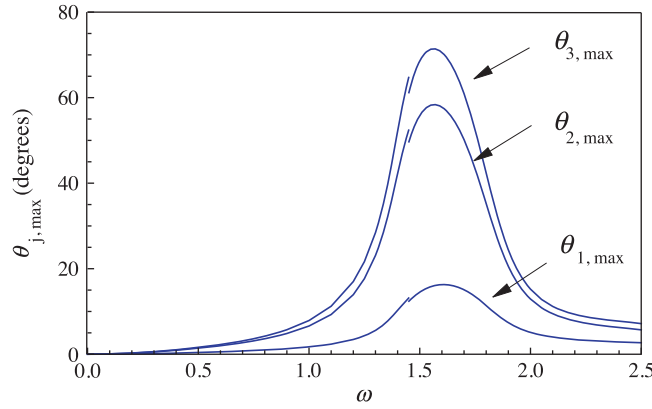


Fig. 3. Triple compound pendulum;  $\theta_{1,\max}, \theta_{2,\max}, \theta_{3,\max}$  vs.  $\omega$  for  $k_1 = 1.0$ ,  $k_2 = k_3 = 0.05$ ,  $c_1 = c_2 = c_3 = 0.1$ ,  $d = 0.1$ .

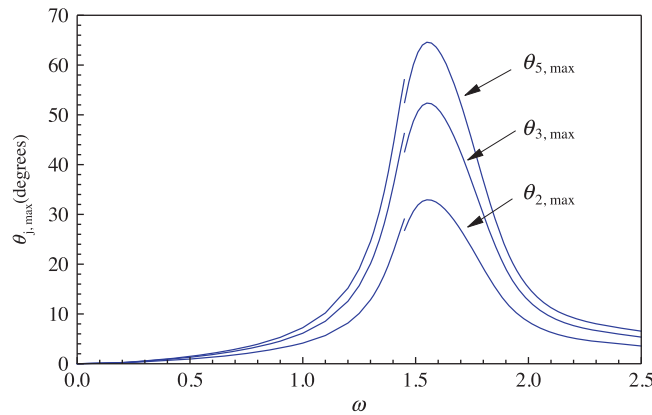


Fig. 4. Five-bar compound pendulum;  $\theta_{2,\max}, \theta_{3,\max}, \theta_{5,\max}$  vs.  $\omega$  for  $k_1 = 15$ ,  $k_2 = k_3 = k_4 = k_5 = 0.15$ ,  $c_1 = c_2 = c_3 = c_4 = c_5 = 0.17$ ,  $d = 0$ .

## 6. Five-bar compound pendulum

Now consider the case  $n=5$ , with each bar having length 5 cm and mass  $m/5$ . For parameters  $k_1 = 15, k_2 = k_3 = k_4 = k_5 = 0.15, c_1 = c_2 = c_3 = c_4 = c_5 = 0.17$ , and  $d=0$ , results are shown in Fig. 4. The nondimensional natural frequencies of the linearized, unforced, undamped system are  $\omega = 1.54, 5.90, 14.94, 26.18$ , and  $57.98$ .

The rotation amplitudes  $\theta_{2,\max}, \theta_{3,\max}$ , and  $\theta_{5,\max}$  are plotted versus  $\omega$  in Fig. 4. The rotation  $\theta_1$  of the top bar is less than  $1^\circ$ , and the rotation  $\theta_4$  is slightly less than  $\theta_5$ , with the maximum difference being  $2.7^\circ$ . The largest values of  $\theta_{j,\max}$ ,  $j = 1, 2, 3, 4, 5$ , are  $0.96^\circ, 32.9^\circ, 52.4^\circ, 61.9^\circ$ , and  $64.6^\circ$ , respectively, and occur at  $\omega = 1.60, 1.56, 1.56, 1.55$ , and  $1.56$ .

At low speeds, the bars are almost in-phase with the lateral head motion. Then the phase lags increase, and at  $\omega = 2.5$  the lag for the bottom bar is  $144^\circ$ .

## 7. Spherical (spatial) pendulum

### 7.1. Formulation

A spherical (spatial) pendulum with a concentrated mass  $m$  at the bottom of a rigid massless bar of length  $L$  is considered. Hence the motions will be three-dimensional. Previous studies involving a spherical pendulum with specified motion at the top support include Refs. [6,14,15].

During each step, the speed of walking or running varies with time, and this variation is included here where motions of the ponytail model are not restricted to the coronal plane. The speed is maximum approximately when a foot leaves the ground (toe-off). At that time, the vertical displacement of the head is almost at its minimum value [2].

In the anterior–posterior (forward–backward) direction (i.e., direction of progression), it will be assumed that the dynamic speed  $V_{\text{dyn}}(T)$  of the woman's head is given by

$$V_{\text{dyn}}(T) = V - 0.08 \sin(2\pi fT) \quad (12)$$

in m/s, where  $V$  is the average speed as used previously [2].

Eqs. (1) and (2) will be used to get  $V$  in terms of  $f$ , and Eqs. (3) and (4) will also be applied. The positive direction of the horizontal head motion  $X(T)$  is reversed from before, and is positive to the left when viewing the back of the head. The vertical motion  $Y(T)$  is again positive if downward, and the motion  $Z(T)$  is positive in the opposite direction to the direction of walking or running. The motion  $Z(T)$  is obtained by integrating  $-V_{\text{dyn}}(T)$ . In Eq. (5), the sign on  $X(T)$  becomes negative, and the nondimensional variables are given by Eq. (8) along with  $z=Z/L$ .

Relative to the top support of the pendulum, the coordinates  $\alpha_1$  and  $\alpha_2$  are defined as in Refs. [16,17], and are the angles between the pendulum and the  $X$ - and  $Z$ -axes, respectively. Rotational springs with stiffness coefficient  $K$ , and rotational dashpots with damping coefficient  $C$ , act at the top. The springs are unstretched when the pendulum is vertical (downward) with  $\alpha_1 = \alpha_2 = \pi/2$ . The springs and dashpots rotate with the bar and experience the rotations  $\phi_1$  and  $\phi_2$ , respectively, and corresponding angular velocities, where  $\phi_1 = (\pi/2) - \alpha_1$  and  $\phi_2 = (\pi/2) - \alpha_2$ . The equations of motion will be written in terms of  $\phi_1$  and  $\phi_2$ .

The projections  $R_X, R_Y$ , and  $R_Z$  of the position of the mass along the  $X$ -,  $Y$ -, and  $Z$ -axes, respectively, are

$$\begin{aligned} R_X(T) &= X(T) + L \sin \phi_1(T), \\ R_Y(T) &= Y(T) + L \sqrt{1 - \sin^2 \phi_1(T) - \sin^2 \phi_2(T)}, \\ R_Z(T) &= Z(T) + L \sin \phi_2(T). \end{aligned} \quad (13)$$

The following resisting aerodynamic force  $F_D$  is assumed to act on the mass:

$$F_D = D_m V_m, \quad V_m = [\dot{R}_X^2 + \dot{R}_Y^2 + \dot{R}_Z^2]^{1/2}, \quad (14)$$

where  $D_m$  is the associated damping coefficient and  $V_m(T)$  is the speed of the mass.

The analysis is conducted in terms of nondimensional variables defined in Eq. (8) along with

$$z = \frac{Z}{L}, \quad d_m = \frac{D_m \sqrt{L}}{m \sqrt{g}}. \quad (15)$$

The nondimensional equations of motion in  $\phi_1(t)$  and  $\phi_2(t)$  are obtained with the help of Lagrange's equations. It is convenient to define

$$\gamma = \frac{1}{\sqrt{2} \sqrt{\cos 2\phi_1 + \cos 2\phi_2}}, \quad s_j = \sin 2\phi_j \quad (j = 1, 2). \quad (16)$$

One equation of motion is given by

$$\begin{aligned} &(\ddot{\phi}_1 + d_m \dot{\phi}_1)(\cos^2 \phi_1 + \gamma^2 s_1^2) + (\ddot{\phi}_2 + d_m \dot{\phi}_2) \gamma^2 s_1 s_2 + 2 \dot{\phi}_1^2 \gamma^4 s_1 s_2^2 + 4 \dot{\phi}_1 \dot{\phi}_2 \gamma^4 s_1^2 s_2 \\ &+ 2 \dot{\phi}_2^2 \gamma^2 s_1 (\cos 2\phi_2 + \gamma^2 s_2^2) + c \dot{\phi}_1 + k \phi_1 + \gamma s_1 + (\ddot{x} + d_m \dot{x}) \cos \phi_1 - (\ddot{y} + d_m \dot{y}) \gamma s_1 = 0, \end{aligned} \quad (17)$$

where overdots denote differentiation with respect to  $t$ . The other equation of motion is obtained by replacing  $x$  by  $z$  in Eq. (17) and interchanging subscripts 1 and 2 in Eq. (17).

## 7.2. Numerical results

The case  $L=25$  cm,  $k=1.4$ , and  $c=d_m=0.2$  is considered. The two equal natural frequencies of the linearized, unforced, undamped system are  $\omega = 1.55$ . The resulting steady-state motions of the mass in the range  $0 \leq \omega \leq 2.5$  are symmetric in the coronal plane. The quantity  $x_{\text{max}}$  denotes the maximum nondimensional amplitude of the horizontal component of the motion in the lateral direction (i.e., the maximum value of  $x(t) + \sin \phi_1(t)$ ) and is plotted versus  $\omega$  in Fig. 5. The curve for walking ends at  $\omega = 1.45$ , as before, with  $x_{\text{max}} = 0.403$ .

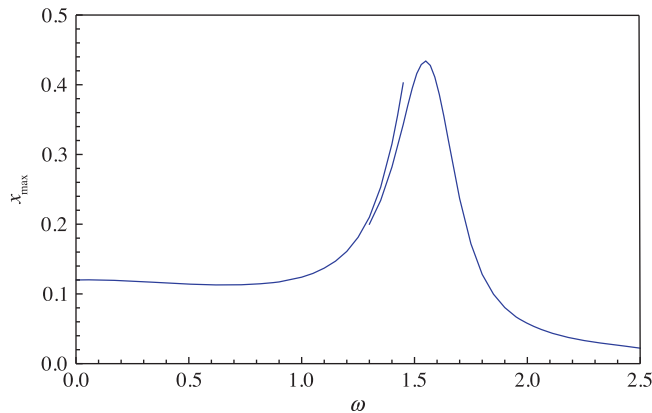


Fig. 5. Spherical pendulum;  $x_{\text{max}}$  vs.  $\omega$  for  $k=1.4, c=d_m=0.2$ .

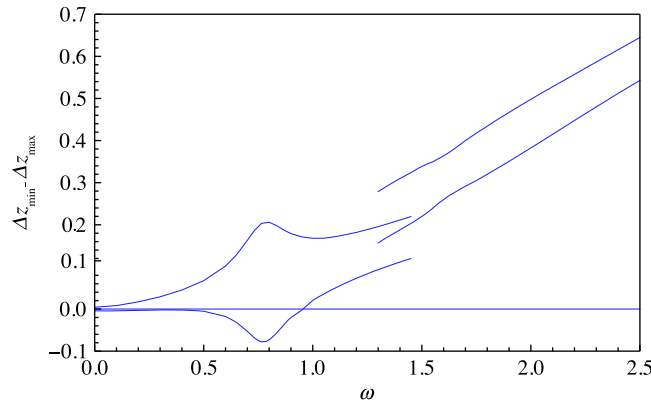


Fig. 6. Spherical pendulum;  $\Delta z_{\max}$  and  $\Delta z_{\min}$  vs.  $\omega$  for  $k = 1.4, c = d_m = 0.2$ .

The curve for running is plotted beginning at  $\omega = 1.3$  ( $f = 2.59$  steps/s), since the typical frequency drop (from  $f = 2.89$  steps/s) at the walk-to-run transition causes a significant change in the motion for this model. At  $\omega = 1.3$ ,  $x_{\max} = 0.200$  on the running curve. The largest value of  $x_{\max}$  occurs at  $\omega = 1.55$  (the natural frequency) and is equal to 0.434.

In the anterior–posterior direction, the nondimensional horizontal motion of the mass is  $z(t)$ , positive if opposite to the direction of motion of the woman. The difference between this motion  $z(t)$  and the motion of the head (i.e., the top support of the pendulum) is denoted  $\Delta z(t)$ , with  $\Delta z_{\max}$  and  $\Delta z_{\min}$  being the corresponding maximum and minimum values, respectively. These quantities are plotted in Fig. 6. In the walking range, when  $\Delta z_{\min}$  is sufficiently negative, the pendulum model may contact the walker's back and in that case the results in Figs. 5 and 6 would not be valid.

Unlike  $\phi_1(t)$  and the horizontal component of lateral motion, the steady-state solutions for  $\phi_2(t)$  and  $z(t)$  have the frequency  $2\omega$  of the vertical and anterior–posterior components of the head motion. The plot of  $\Delta z_{\max}$  in Fig. 6 has a local maximum  $\Delta z_{\max} = 0.207$  at  $\omega = 0.788$  (i.e., at approximately half the natural frequency). In the running range,  $\Delta z_{\max}$  and  $\Delta z_{\min}$  increase almost linearly with  $\omega$  in Fig. 6, i.e., the ponytail model tends to move away from the body as the running speed increases.

## 8. Experiments on double compound pendulum

Experiments were conducted on a double compound pendulum with two aluminum strips, each having length 15.24 cm, width 2.54 cm, thickness 0.16 cm, and weight  $m_1g = 0.163$  N. The double pendulum is shown in the schematic in Fig. 7(a) and the photograph in Fig. 7(d). The centers of the holes for the top hinge and connecting hinge were located 0.95 cm from the ends of the strips.

A relatively high-speed video camera (Prosilica GC640) was used to track the motion of three points, labeled A, B, and C in Fig. 7(a). Point A, the top pivot point, followed the path of the externally applied motion. Point B was at the connecting hinge and point C was close to the bottom of the double pendulum. The optical tracking software (implemented via LabVIEW) followed the motion of the three targets and converted from the horizontal and vertical locations in pixels to the rotations  $\theta_1(T)$  and  $\theta_2(T)$  using MATLAB.

The damping behavior of the system was examined by giving each bar an initial angle of about  $60^\circ$  from the vertical and observing the resulting time series. The plots of the angles in this free decay are shown in Fig. 7(b,c). The bars essentially maintained equal angles and acted like a single pendulum, and the damping was very light. The fundamental natural frequency was estimated to be 1.15 Hz, and the decay envelope was almost linear, implying that Coulomb damping (friction) might be the dominant mechanism. Initial conditions with the bar angles having opposite signs were also investigated.

For the numerical modeling of the experiments, Eq. (7) was applied with no rotational springs, rotational dashpots, or aerodynamic damping. Friction was modeled at the joints. The frictional resisting moment at the top is  $M_1(T) = M_{F1} \operatorname{sgn}(d\theta_1/dT)$ , i.e., it has magnitude  $M_{F1}$ , acts clockwise when  $d\theta_1/dT > 0$ , and acts counter-clockwise when  $d\theta_1/dT < 0$ . At the hinge between the two bars, the frictional moment is  $M_2(T) = M_{F2} \operatorname{sgn}(d\theta_2/dT - d\theta_1/dT)$ . Then  $M_1(T) - M_2(T)$  was added to the left side of Eq. (7) for  $i = 1$ , and  $M_2(T)$  was added to the left side of Eq. (7) for  $i = 2$ .

In the numerical solution, the signum function  $\operatorname{sgn}(\rho)$  was approximated by  $\rho/[(\rho^2 + 0.0001)^{1/2}]$ . The amplitudes  $M_{F1}$  and  $M_{F2}$  were assumed to be equal, and a comparison of the experimental and numerical free-decay motions led to the value  $M_{F1} = M_{F2} = 0.02m_1gL_0$  where  $L_0 = 13.3$  cm is the distance between the top pivot and the connecting hinge. This furnishes the value  $M_{F1} = M_{F2} = 0.0434$  N cm.

In the experiments, the upper pivot was attached to a Scotch-yoke mechanism, as seen in Fig. 8. This device provided harmonic horizontal motion, which was converted to a parabolic motion in the vertical plane via two guides (Fig. 8(b,c)) and a sliding shaft within a cylinder (Fig. 8(c)). Fig. 8(d) shows a measurement of the pivot motion profile, using the digital



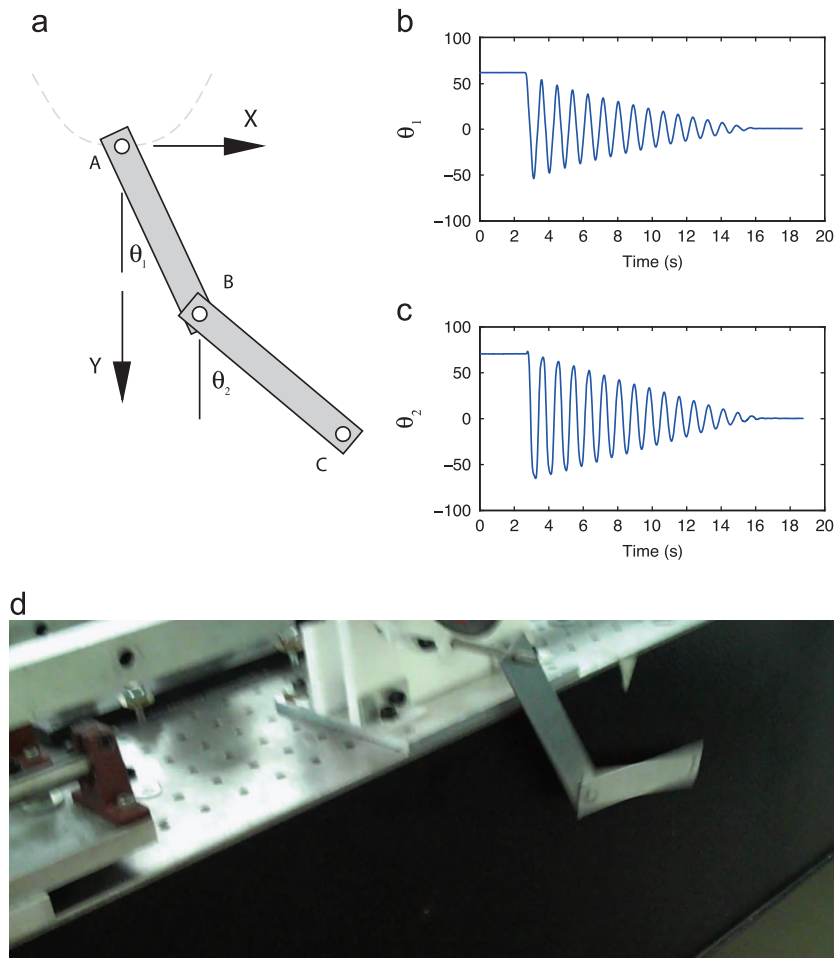


**Fig. 7.** (a) Schematic of the two-bar pendulum, (b) and (c) free decays for  $\theta_1$  and  $\theta_2$ , respectively, (d) photographic image of the experimental system.

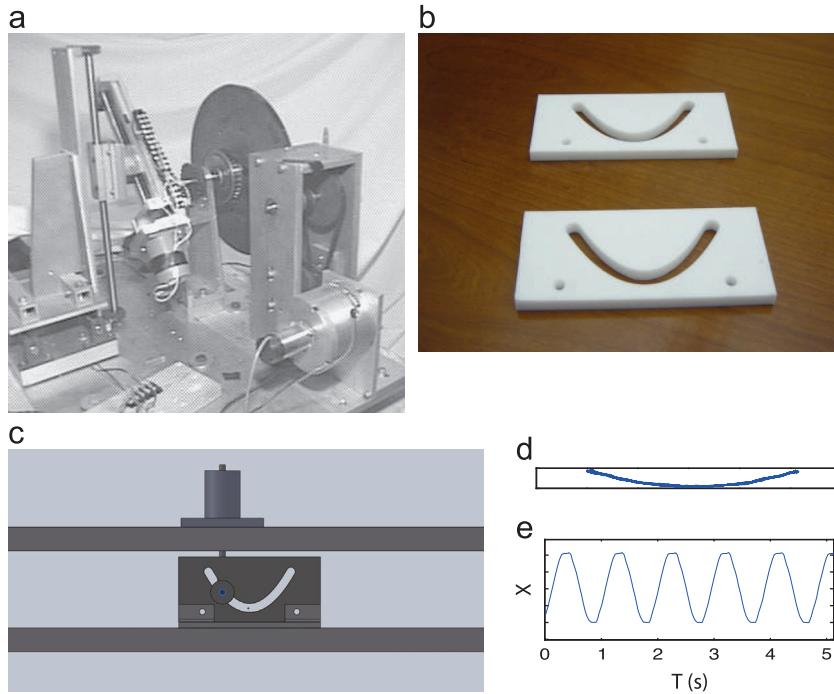
camera mentioned above at a rate of 100 frames/s. The equation of this path is given by  $Y = -X^2/10.16$  if  $X$  and  $Y$  are in cm ( $Y = -X^2/4$  if  $X$  and  $Y$  are in inches) and for the specific profile shown corresponded to a peak-to-peak amplitude of 3 cm in the horizontal ( $X$ ) direction and a vertical peak-to-peak amplitude of about 2.2 mm. A deeper parabolic forcing, with the vertical amplitude twice as large, was also tested. A time series of the measured horizontal motion of the point A is shown in Fig. 8(e) for a forcing frequency close to the fundamental natural frequency of the system.

In the forced experiments, the horizontal forcing peak-to-peak amplitude was held fixed at 3 cm throughout, and data were acquired for different forcing frequencies over the range 0.6–2.4 Hz (horizontal cycles per second), within which the Scotch-yoke worked well. (In Figs. 9–12 and the remainder of this section, “frequency” and “ $f$ ” will refer to horizontal frequency in Hz, rather than vertical frequency.) After waiting for transients to decay, many cycles of data were then recorded and the maximum values of the bar rotations were extracted using post-processing (similar to the procedure used in the simulations via Mathematica).

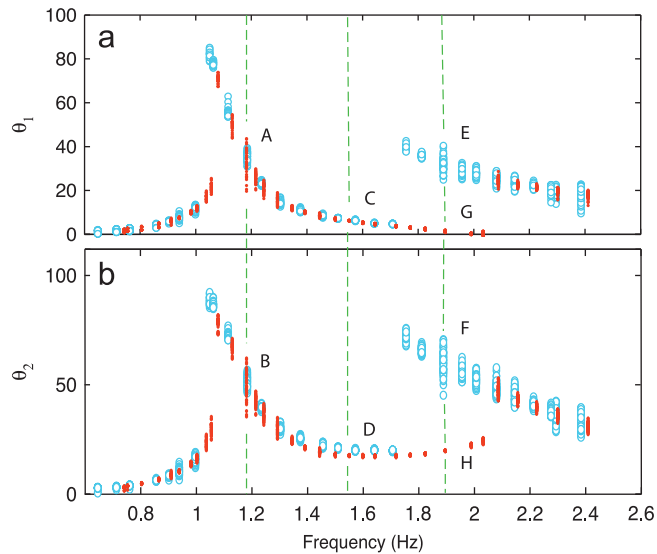
Fig. 9 shows an experimental frequency-response diagram. These results correspond to the shallower parabolic forcing, but are not qualitatively different from the deeper parabolic forcing results. The main resonant peak occurs at a little over 1 Hz (the natural frequency is 1.15 Hz) with a mild softening effect apparent. There are also significant hysteresis effects over the frequency range 1.7–2.1 Hz. The small red data points correspond to data acquired during a very slow sweep up in forcing frequency, and the larger open blue data points are obtained from a sweep down. Some sample time series are shown in Fig. 10 and are indicated by the vertical dashed green lines in Fig. 9. Although most of the oscillations are nearly periodic, there are some ranges of forcing frequency for which the behavior exhibits beating, e.g., the increased spread of data at a forcing frequency of 1.18 Hz. This was also observed in simulations, but in both cases the beats died out over time. The other area in which there is a noticeable “spread” in the oscillation is typified by the time series labeled E and F. However, this region of response is more random-like in nature. At this value of forcing frequency, these oscillations co-exist with a small-amplitude oscillation (time series G and H) that is much more periodic.

Fig. 11 shows the same experimental data but with the numerical result superimposed. The agreement is good. Fig. 12 shows another comparison between experimental data and numerical simulation. These plots display the two





**Fig. 8.** (a) Scotch-yoke forcing mechanism, (b) guide grooves for support motion, (c) schematic of top support, (d) measured top pivot motion, (e) time series of the horizontal projection of top pivot motion.



**Fig. 9.** Frequency response of the experimental system in terms of maximum amplitude, (a) upper arm,  $\theta_1$ , (b) lower arm,  $\theta_2$ . The small (red) dots correspond to a sweep-up in frequency, and the larger open (blue) data points correspond to a sweep down. (For interpretation of the references to color in this figure caption, the reader is referred to the web version of this article.)

angles plotted against each other (configuration space) for representative forcing frequencies. Experimental results are shown on the left-hand side, numerical results on the right. The phase difference between the two arms can be readily discerned, as well as the inevitable noise present in the experimental results. There are two co-existing responses in the region of hysteresis, for example when  $f=1.9$  Hz, and these cases thus depend on initial conditions. On the upper-right curve in each part of Fig. 11, instead of rotating together, one bar tends to rotate to the left when the other rotates to the right (i.e.,  $\theta_1$  and  $\theta_2$  tend to have opposite signs). This is seen in the phase projections in Fig. 12(e,f) associated with each of those curves at  $f=1.9$ .

In addition to the conventional modeling issues of matching the physical parameters, e.g., damping or natural frequencies, the mild discrepancies between the experimental and numerical data are caused by a number of factors: there

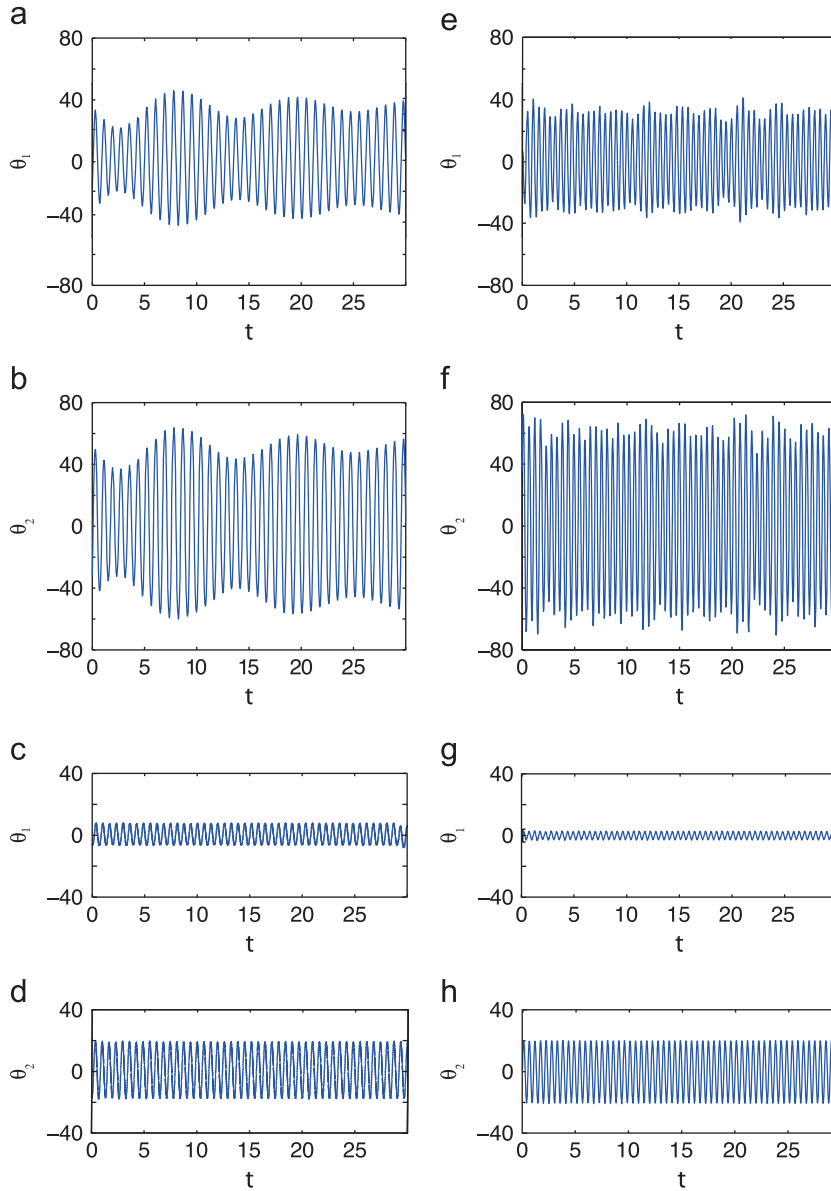


**Fig. 10.** Sample experimental time series, (a)  $\theta_1$  at  $f=1.18$  Hz, (b)  $\theta_2$  at  $f=1.18$  Hz, (c)  $\theta_1$  at  $f=1.55$  Hz, (d)  $\theta_2$  at  $f=1.55$  Hz, (e)  $\theta_1$  at  $f=1.9$  Hz, (f)  $\theta_2$  at  $f=1.9$  Hz, (g)  $\theta_1$  at  $f=1.9$  Hz, (h)  $\theta_2$  at  $f=1.9$  Hz.

is a small foreshortening angular error from the camera offset; the motions of the Scotch yoke and guide tracks are not perfectly sinusoidal; inevitable standard (Gaussian) precision errors occur in the measurements; extracting the maximum values from an oscillation with finite resolution may involve a small error; many forcing cycles are superimposed in the data; in general the transients were very long, primarily due to the light damping, and thus a small amount of transient motion may be included; and capturing the ends of the hysteresis region is especially challenging, since the approach of a saddle-node bifurcation (amplitude jump) is accompanied by a rapid shrinking of the local basin of attraction and hence enhanced sensitivity to small perturbations.

## 9. Concluding remarks

The dynamic behavior of ponytails during walking and running has been investigated. The head moves vertically and sideways as well as forward, and applies external and parametric excitation to the top of the ponytail. The relationships of step frequency to average walking or running speed, given in Eqs. (1) and (2), were not utilized in the numerical examples. However, they are useful so that the numerical results presented in terms of frequency can be related to the speed of walking or running. The head motions were based mainly on data from adult women, and would tend to be larger for men.

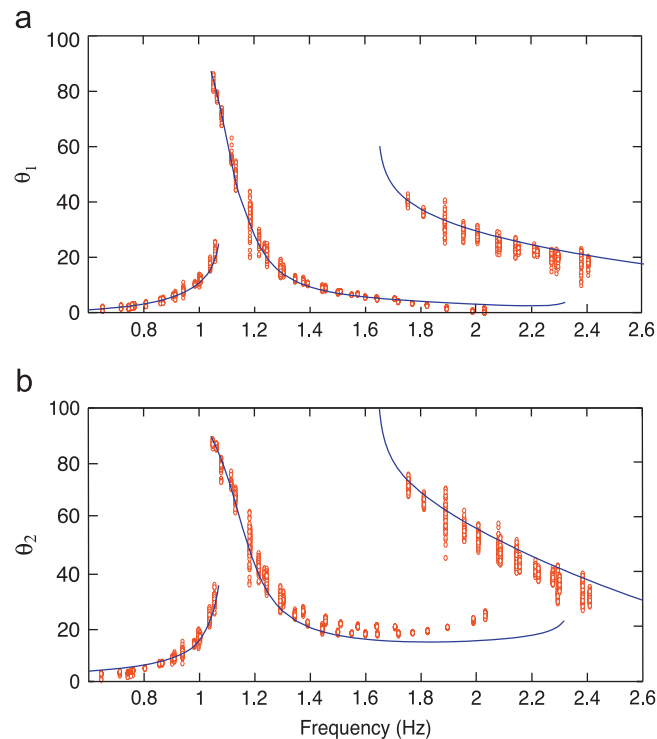


**Fig. 11.** Frequency response of the experimental system with numerical results superimposed, (a) maximum angle (amplitude) of the upper arm,  $\theta_1$ , (b) maximum angle (amplitude) of the lower arm,  $\theta_2$ .

In most of the examples the ponytail was modeled as a single compound pendulum or a pendulum comprised of a number of rigid bars pinned together, with rotational springs and dashpots acting at the joints and with aerodynamic damping. Stable steady-state motions with constant amplitude were analyzed, using numerical integration of the equations of motion. Attention was focused on the effect of the step frequency on the maximum amplitude. Numerical results were presented for pendulum models with one, two, three, or five bars. Planar motions perpendicular to the direction of progression were examined except for an example of a spherical pendulum, where three-dimensional motions were investigated.

Based on observation, the peak motions tend to occur when the woman is jogging (i.e., running slowly), and their rotations tend to be less than  $90^\circ$ . The stiffness and damping coefficients were chosen to satisfy these characteristics in the numerical examples. The resulting motions had the period of the sideways motion of the head, which is twice the period of the vertical motion. In the sideways direction, the responses were symmetric. In general, as the step frequency increased, the ponytail oscillations tended to lag further behind the sideways head motion.

Any contact between the ponytail and the woman's back was neglected. In the example of a spherical pendulum, the ponytail moved forward relative to its top support for part of the walking range, so that such contact might occur. This feature could be included in a future analysis (e.g., see Refs. [18,19]).

Experiments were conducted on a double compound pendulum. The applied motion at the top was parabolic, which is similar to head motions in the coronal plane during running, and its amplitude was fixed as the forcing frequency was varied. The amplitudes of the aluminum bars jumped from around  $30^\circ$  to approximately  $90^\circ$  when the forcing frequency was increased past the fundamental frequency. For a higher range of frequency, two stable steady-state solutions co-existed, with the rotation angles tending to have opposite signs on the branch with higher amplitudes. In numerical modeling of the experiment, dissipation of energy was represented by frictional resisting moments at the joints. The experimental and numerical results demonstrated good agreement over most of the frequency range.

In Ref. [4], an example of a double pendulum is analyzed in which the support motion is larger than for a typical walker or runner. Symmetry-breaking is demonstrated and asymmetric motions occur in two ranges of speeds. Also, erratic and complex motions are exhibited.

The type of problem considered here, compound or multi-bar pendulums with an oscillating support, appears in a number of applications. One is a floating crane or a crane on a ship, subjected to wave excitation [20]. Some others involve pendulum vibration absorbers, such as on helicopter blades [21], mounted on crankshafts in engines [22], or used to mitigate the seismic response of buildings [23].

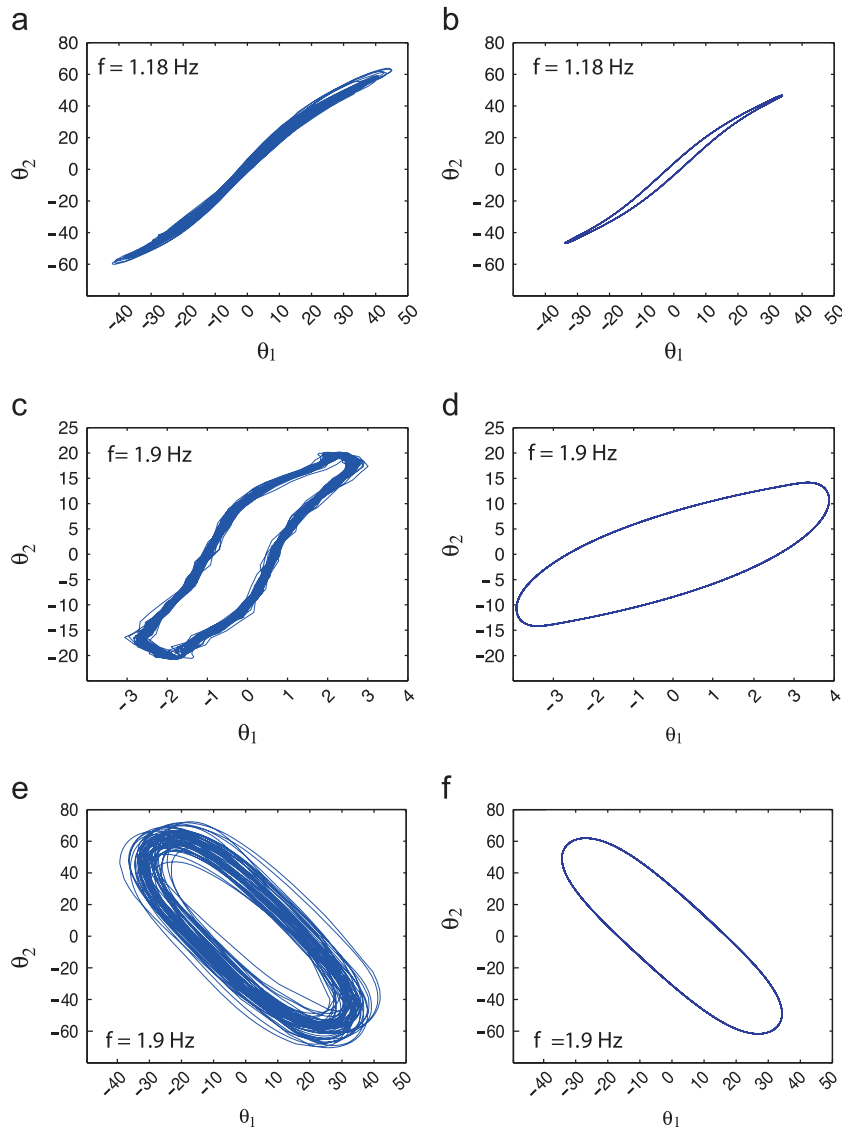


**Fig. 12.** Phase projections plotting the two pendulum arms against each other for various forcing frequencies. Experimental: (a)  $f=1.18$  Hz, (c)  $f=1.9$  Hz, (e)  $f=1.9$  Hz (upper branch); numerical: (b)  $f=1.18$  Hz, (d)  $f=1.9$  Hz, (f)  $f=1.9$  Hz (upper branch).

## References

- [1] J.B. Keller, Ponytail motion, *SIAM Journal on Applied Mathematics* 70 (7) (2010) 2667–2672.
- [2] R.H. Plaut, Head deflections during walking and running, *Human Movement Science*, under review.
- [3] A.H. Nayfeh, D.T. Mook, *Nonlinear Oscillations*, Wiley, New York, 1979.
- [4] R.H. Plaut, L.N. Virgin, Pendulum models of ponytail motion during walking and running, Technical Report CE/VPI-ST-12/11, Structural Engineering and Materials, Department of Civil and Environmental Engineering, Virginia Tech, 2012.
- [5] M.E. Bacon, D.D. Nguyen, Real-world damping of a physical pendulum, *European Journal of Physics* 26 (4) (2005) 651–655.
- [6] O. Gottlieb, G. Habib, Non-linear model-based estimation of quadratic and cubic damping mechanisms governing the dynamics of a chaotic spherical pendulum, *Journal of Vibration and Control* 18 (4) (2012) 536–547.
- [7] M. Braun, On some properties of the multiple pendulum, *Archive of Applied Mechanics* 72 (11–12) (2003) 899–910.
- [8] P. Fritzowski, H. Kaminski, A discrete model of a rope with bending stiffness or viscous damping, *Acta Mechanica Sinica* 27 (1) (2011) 108–113.
- [9] Q. Zhu, M. Ishitobi, Experimental study of chaos in a driven triple pendulum, *Journal of Sound and Vibration* 227 (1) (1999) 230–238.
- [10] J. Galán, W.B. Fraser, D.J. Acheson, A.R. Champneys, The parametrically upside-down rod: an elastic jointed pendulum model, *Journal of Sound and Vibration* 280 (1–2) (2005) 359–377.
- [11] I. Rivas-Camero, J.M. Sausedo-Solorio, Dynamics of the shift in resonance frequency in a triple pendulum, *Meccanica* 47 (4) (2012) 835–844.
- [12] G.L. Baker, J.A. Blackburn, *The Pendulum: A Case Study in Physics*, Oxford University Press, Oxford, 2005.
- [13] M. Gitterman, *The Chaotic Pendulum*, World Scientific, Singapore, 2010.
- [14] A.Y.T. Leung, J.L. Kuang, On the chaotic dynamics of a spherical pendulum with a harmonically vibrating suspension, *Nonlinear Dynamics* 43 (3) (2006) 213–238.

- [15] J.H.E. Cartwright, D.J. Tritton, Chaotic dynamics and reversal statistics of the forced spherical pendulum: comparing the Miles equations with experiment, *Dynamical Systems* 25 (1) (2010) 1–16.
- [16] L.N. Virgin, R.H. Plaut, Use of frequency data to predict secondary bifurcation, *Journal of Sound and Vibration* 251 (5) (2002) 919–926.
- [17] D. Orlando, P.B. Gonçalves, G. Rega, S. Lenci, Influence of modal coupling on the nonlinear dynamics of Augusti's model, *Journal of Computational and Nonlinear Dynamics* 6 (4) (2011) 041014.
- [18] P.V. Bayly, L.N. Virgin, An experimental study of an impacting pendulum, *Journal of Sound and Vibration* 164 (2) (1993) 364–374.
- [19] L.N. Virgin, C.J. Begley, Grazing bifurcations and basins of attraction in an impact-friction oscillator, *Physica D* 130 (1–2) (1999) 43–57.
- [20] K.-P. Park, J.-H. Cha, K.-Y. Lee, Dynamic factor analysis considering elastic boom effects in heavy lifting operations, *Ocean Engineering* 38 (10) (2011) 1100–1113.
- [21] I. Nagasaka, Y. Ishida, T. Koyama, Vibration suppression of helicopter blades by pendulum absorbers (first elastic mode of the blade), *Sixth EUROMECH Nonlinear Dynamics Conference ENOC-2008*, Saint Petersburg, Russia, 7 pp.
- [22] D.L. Cronin, Shake reduction in an automobile engine by means of crankshaft-mounted pendulums, *Mechanism and Machine Theory* 27 (5) (1992) 517–533.
- [23] E. Matta, A. De Stefano, Robust design of mass-uncertain rolling-pendulum TMDs for the seismic protection of buildings, *Mechanical Systems and Signal Processing* 23 (1) (2009) 127–147.